Study of the Air-Sea Momentum Flux of the Coastal Marine Boundary Layer During Typhoons

Qilong Li[1], Xueling Cheng[2], Xiaodong Zeng[1], Guangqing Zhou[1], Jian Huang[3], Lin Wu[2], and Qingcun Zeng[2]

[1]Institute of Atmospheric Physics
[2]Institute of Atmospheric Physics, Chinese Academy of Sciences
[3]Institute of Tropical and Marine Meteorology, CMA

November 22, 2022

Abstract

We analyzed the variations in the mean wind field, turbulence, and turbulent flux at the landfall sites of three typhoons using observational data obtained from an offshore monitoring platform. These variations were different for onshore and offshore winds. The turbulent fluctuation intensity and friction velocity increased with wind speed both before and after landfall. However, the turbulent flow decreased with increasing wind speed during landfall. The relationships between the friction velocity and drag coefficient and the wind speed were affected by whether the typhoon makes landfall, and the relative position of the landfall site of the typhoon and the observation site.

Study of the Air-Sea Momentum Flux of the Coastal Marine Boundary Layer During Typhoons

Qilong Li[1], Xueling Cheng[1,2], Xiaodong Zeng[1], Guangqing Zhou[1], Jian Huang[3], Lin Wu[1], Qingcun Zeng[1]

[1] Institute of Atmospheric Physics, Chinese Academy Sciences, Beijing, China

[2] College of Earth Science, University of Chinese Academy of Sciences, Beijing, China

[3] Institute of Tropical and Marine Meteorology, China Meteorology Administration, Guangzhou, China,

Corresponding author: Xueling Cheng (chengxl@mail.iap.ac.cn)

Abstract

We analyzed the variations in the mean wind field, turbulence, and turbulent flux at the landfall sites of three typhoons using observational data obtained from an offshore monitoring platform. These variations were different for onshore and offshore winds. The turbulent fluctuation intensity and friction velocity increased with wind speed both before and after landfall. However, the turbulent flow decreased with increasing wind speed during landfall. The relationships between the friction velocity and drag coefficient and the wind speed were affected by whether the typhoon makes landfall, and the relative position of the landfall site of the typhoon and the observation site.

Plain Language Summary

Winds blowing across the surface of the sea cause waves, which, in turn, affect the wind flow. This interaction has been well defined at low wind speeds, but has not previously been studied for strong winds such as typhoons. We found that this interaction is related to landfall site of the typhoon and may be different from the interaction at low wind speeds. By analyzing the turbulent data get from the costal platform during typhoons, an interesting phenomenon was observed. The relationships between the turbulence fluctuation intensity, the friction velocities, the drag coefficients and wind speed at 10 m height are not completely distinguished by the wind direction such as onshore wind and offshore wind, but by the process of before, during and after landfall of the typhoon.

1 Introduction

The momentum flux of the air-sea interface—namely, the sea surface wind stress—is the main force driving the circulation and waves in the upper ocean. In general, the sea surface wind stress can be parameterized by the drag coefficient C_d or the aerodynamic roughness length z_0 in. Therefore, the study of sea surface wind stress becomes into the study of C_d or z_0 under neutral conditions. For land atmospheric boundary layer, corresponding to theoretical research on the boundary layer between the land and the atmosphere is relatively mature. The two forms of wind profile—the power law and logarithmic forms—are based on the underlying surface (roughness elements) of the land-atmosphere boundary layer. The aerodynamic roughness is determined in a similar way and there is a relationship between these two parameters; importantly, the underlying land surface does not change when the wind speed changes. The marine atmospheric boundary layer is different. The roughness elements (e.g., waves, sea sprays) on the underlying surface are strongly influenced by the wind and change according to the wind speed. These waves cause fluctuations in the sea surface and the air flow close to the surface also fluctuates, causing a wave-generated Reynolds stress, which will affect the wind stress of the sea surface. Sea sprays accelerate to the local wind speed when they thrown into the air. When these droplets then crash back into the sea, they transfer their momentum to the sea surface as a surface stress (Andreas, 2004). Thus, the factors affecting the aerodynamic roughness of the sea surface are therefore complex because they not only vary with the wind speed, but are also affected by the waves on the underlying surface.

Much research has been carried out on the sea surface wind stress (Donelan, 1990; Drennan et al., 2003; Geernaert, 1987; Johnson et al., 1998; Lange et al., 2004; Smith et al., 1992; Stewart, 1974; Toba et al., 1990; Wu, 1980; Yelland & Taylor, 1996; Taylor & Yelland, 2001). However, most of these studies were limited to low wind speeds and coarse air-sea interactions. The relationship between C_d or z_0 and the 10 m wind speed, wave age, wave steepness, velocity, relative direction of wind waves, and swell have all been studied under these conditions (Donelan et al., 1993; Garratt, 1977; Large & Pond, 1981; Smith, 1988; Taylor & Yelland, 2001; Vickery & Skerlj, 2000). It is always difficult for the air-sea interface flux calculation under strong wind condition and the block formula used has large errors at high wind speeds. The momentum exchange for strong winds is calculated by the drag coefficient, which is dependent on the sea state. C_d is used as a function of the wind speed to parameterize the surface stress, but there have been few observations for the open ocean with wind speeds >20 m s^{-1} at a height of 10 m.

The increase in the bulk transfer coefficients for heat (C_H) and moisture (C_E) with wind speed is also uncertain. The TOGA-COARE block algorithm, which is considered to be the most accurate method of flux parameterization, is only currently applicable when the wind speed is <15 m s^{-1}. When the wind speed is >15 m s^{-1}, the C_d values of COARE 3.0 and the National Center for Environmental Prediction are different from the observed values. Andreas & Decosmo (1999) analyzed sensible and latent heat data from the HEXOS (Humidity Exchange over the Sea) program and showed that the surface latent heat flux was significantly underestimated when the wind speed reached 20 m s^{-1}, which could be extended to 15 m s^{-1} after considering the effect of ocean droplets.

The study of the air-sea flux at high wind speeds has developed greatly in recent years with improvements in detection methods. Ishizaki (1983) analyzed the typhoon wind velocity, wind profile exponent, and turbulence intensity and found that the power law exponent and turbulence intensity decreased with increasing wind speed. High-resolution wind profile measurements are now possible as a result of the development of the Global Positioning System dropwindsonde (Hock and Franklin, 1999). Powell et al. (2003) analyzed a large number of wind speed profiles measured by a falling GPS dropwindsonde in tropical cyclones and showed that the mean wind speed increases logarithmically with height in the lowest 200 m, reaching a maximum near 500 m and decreasing gradually up to a height of 3 km. The drag coefficient decreases with increasing wind speed when the wind speed is >33 m s^{-1} and the sea surface roughness also decreases with an increase in wind speed at high wind speeds. This may be due to the existence of a layer of foam formed by breaking waves and wind shear on the sea surface at high wind speeds.

Gao et al. (2000) calculated the aerodynamic roughness and neutral drag coefficient under different sea surface conditions based on observed data for atmospheric turbulence near the surface of the Subi Reff in 1994. Cao et al. (2009) studied Typhoon Maemi and found that the turbulence intensity of the easterly wind was greater than that of the westerly wind. In addition, the turbulence intensity of the onshore wind was greater than that of the offshore wind with the same wind speed at the same location. Song et al. (2016) analyzed three typhoons (Haguit, Nesat, and Rammasun), the core regions of which passed across six towers. They examined the structural evolution of the typhoon wind profiles and found the impact of different surface roughness values on the wind profile exponent. There are also studies on the characteristics of Typhoon Hagupit based on aircraft observations over the sea surface (Harper et al., 2008; Sparks, 2003; Sparks & Huang, 2001).

Zhao et al. (2015) investigated the air-sea drag coefficient during typhoon landfalls based on multilevel wind measurements from a coastal tower located in the South China Sea. They found that the plot of C_d against the wind speed of the typhoon is similar to that of open ocean conditions. However, the C_d curve shifts toward a regime of lower winds and increases by a factor of about 0.5 relative to the open ocean. These findings were explained by shoaling effects. A formula for C_d dependent on water depth may be particularly pertinent for parameterizing air-sea momentum exchanges over shallow water. Tamura et al. (2007) found that the wind shear of inland stations at different distances from the coastline is different during an onshore wind, and the wind shear of stations closer to the coast is smaller. Fang et al. (2018) studied the effects of wind direction on variations in friction velocity with wind speed under moderate (≥9 m/s) to strong (≥22 m/s) onshore wind conditions using 20-Hz ultrasonic wind data from a coastal tower at three different heights. They pointed out that wind direction have an important effect on the variations in friction velocity with U_{10}. However, their observation points are on the land side. In the case of strong wind, how small the wind shear is at the observation points on the sea, and how the friction velocity changes with the wind direction? We used data obtained from the tower on a platform about 6.5 km from the coast in the South China Sea during typhoon landfalls and analyzed the relationships between the turbulence fluctuation intensity, friction velocities, drag coefficients, and wind speed at 10 m height. We found that the wind profile is almost unchanged, but the relationships are not only related to wind direction but also different before, during, and after landfall of the typhoon.

2 Site and equipment

The Bohe Maoming Integrated Observation Platform for Marine Meteorology is located 6.5 km offshore in the South China Sea at (21 °26′ 24" N, 111 °23' 26" E) (Bi et al., 2015) in a water depth of 15 m. The observation platform is located about 11 m above average sea level. The upper part of the platform is a 25-m high steel tower. The wind speed sensor (model RM young/05106), temperature and humidity sensor (model HMP45C) are installed on 2-m booms at five different heights (13, 16, 19, 23, and 31 m above sea level). The sampling frequency is every 1 min. Gill Windmaster Pro ultrasonic anemometers are installed on booms 27 and 35 m above the sea surface and the sampling frequency is 10 Hz (Zhao et al., 2013). Figure 1 shows the location of the Bohe offshore platform and the observation tower on the platform. The instruments are installed on the east side of the tower, facing the sea, to minimize the impact of the tower body on the wind flow.

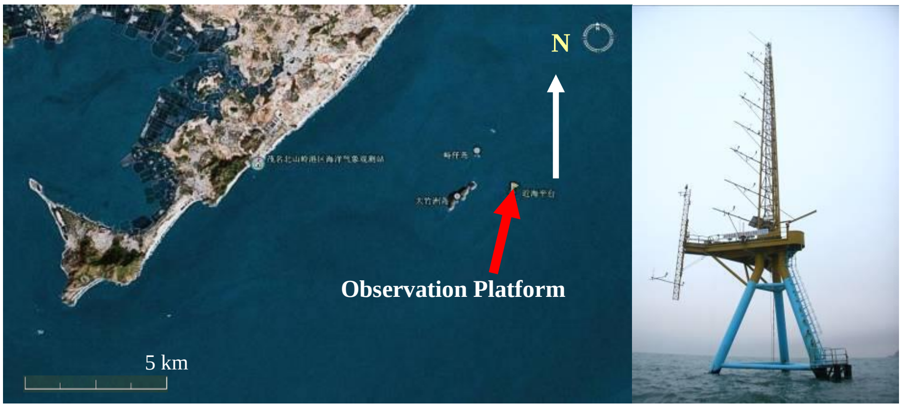

Figure 1. Location of the observation platform at Bohe.

3 Data and methods

We analyzed three typhoons that made landfall in Guangdong. Typhoon Koppu formed on the sea surface in the northern Philippines in the early morning of 13 September 2009. It strengthened to a severe tropical storm at 1000 h (Beijing time) on 14 September and then to a typhoon at 1700 h. The typhoon made landfall in Taishan, Guangdong (21.8 °N, 112.4 °E) at 0700 h on 15 September. It then weakened to a severe tropical storm at 1000 h, a tropical storm at 1400 h, and a tropical depression at 2300 h. Typhoon Chanthu formed on 19 July 2010 and strengthened to a typhoon at 1700 h on 21 July. It made landfall in Wuchuan, Guangdong (21.3 °N, 110.8 °E) at 1345 h on 22 July and weakened to a strong tropical storm at 1900 h. It weakened to a tropical storm and then a tropical depression in western Guangxi at 1700 h on 23 September. Typhoon Hato formed over the northwest Pacific Ocean at 1400 h on 20 August 2017 and strengthened to a severe tropical storm at 0800 h on 22 August and then to a typhoon at 1500 h. It intensified to a strong typhoon at 0700 on 23 August, with the strongest winds reaching 48 m s^{-1} at about 1250 h. It made landfall at Zhuhai (22 °N, 113.2 °E) as a strong typhoon (level 14, 45 m s^{-1}) and then weakened to a tropical depression at 1400 h on 24 August.

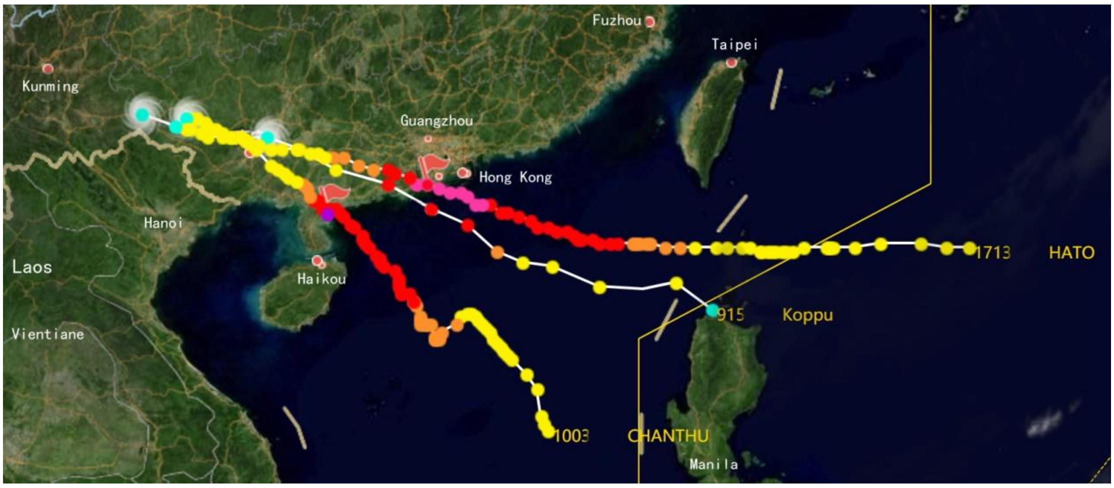

Figure 2. Paths of Typhoons Hato, Koppu, and Chanthu.

We carried out quality control procedures on the ultrasonic wind temperature data, taking into account the harsh observational conditions of high temperatures, high salinity, high humidity, and high wind speeds during the passage of the typhoon over the ocean, the location of the observation platform 6.5 km offshore and the limited power supply during the typhoon. These procedures included removing data that were significantly inconsistent with the statistical characteristics, exceeded variable thresholds, or had no physical significance. We eliminated outliers and random pulsations and carried out tests for amplitude resolution, stiffness, high-order statistical (Vickers & Mahrt, 1997) and stationarity (Foken & Wichura, 1996).

According to the measuring range of the instrument, the wind speed thresholds were [−65 m s^{-1}, 65 m s^{-1}] and the temperature thresholds were [−40℃, 70℃]. Excluding the random pulses caused by the condensation of water vapor on the sensor and considering that there are many asymmetries in the probability density distribution of atmospheric turbulence (Quan et al., 2007), we used a non-Gaussian distribution (Ma & Hu, 2004) to protect the original data and took the confidence interval as 5σ—that is, random pulsation outside the interval [-5σ, $+5\sigma$].

When the resolution of the amplitude of a sequence is too small to capture turbulent fluctuation, this leads to the appearance of a stepped time sequence. The low resolution may also be related to the abnormal operation of the instrument or the data processing system. When the position of zero in the probability density function of a sequence is >70%, the resolution of the amplitude of the sequence is considered to be too low and fails the amplitude resolution test.

Problems with the ultrasound probe and data recording system may result in minimal changes in the data for a continuous period of time, resulting in a stiff value. When the difference between adjacent points is less than a certain threshold, then this is considered to be a stiff value. The threshold can be selected as the width of the bin of the probability density function of the time series. The number of bins is usually taken to be 100 and the width of the bin is [max(x)−min(x)]/100, where x is the data point to be tested. The time for each stiffness test is 10 min.

If the high-order statistical moments of the data are abnormally large or small compared with the Gaussian distribution, then this may mean that there is a problem with the instrument and the data recording system. We calculated the skewness S and kurtosis K of the data, which are defined as follows:

$$\begin{aligned} S &= \frac{E(x-\mu)^3}{\sigma^3} \\ K &= \frac{E(x-\mu)^4}{\sigma^4} \end{aligned}, \tag{1}$$

where σ is the sample variance and μ is the sample average. The sequence is considered to have failed the high-order statistical moment test when the absolute value of S is >2, the value of K is >8, or the value of K is <1.

Stationarity occurs when various statistical characteristics of the turbulence field do not change with time. Almost all statistical theories of turbulence are based on the assumption of the stationarity of the turbulence field. The actual atmospheric turbulence field is affected by diurnal changes or weather systems and therefore, strictly speaking, it does not have the characteristics of stability. However, if we take a shorter observation time, then the atmospheric turbulence can be approximately regarded as stable. The data to be tested can be divided into M segments (M is generally selected as 4–8 and the default value is 6) and the covariance of each segment is calculated separately:

$$(\overline{x'w'})_i = \frac{1}{N-1}\left[\sum_j x_j w_j - \frac{1}{N}\sum_j x_j \sum_j w_j\right], \tag{2}$$

where N is the number of data points in each segment and x and w can be either two different sequences or the same sequence. The former is used to test the stationarity between fluxes (e.g., x is temperature and w is the vertical wind speed) and the latter is used to test the stationarity of the sequence itself. If we find the arithmetic mean of the M covariance, we obtain

$$\overline{x'w'} = \frac{1}{M}\sum_i (\overline{x'w'})_i \,. \tag{3}$$

We then calculate the covariance of the data to be tested before segmentation:

$$(\overline{x'w'})_o = \frac{1}{MN-1}\left[\sum_j x_j w_j - \frac{1}{NM}\sum_j x_j \sum_j w_j\right]. \tag{4}$$

If $\left|\frac{\overline{x'w'} - (\overline{x'w'})_o}{(\overline{x'w'})_o}\right| > 30\%$, then the data are considered to be unstable and fail the stationarity test.

After quality control, the wind speed direction is rotated to the mean wind direction so that u_r in the rotated coordinate system represents the wind speed in the downwind direction, v_r represents the wind speed perpendicular to the downwind direction, and w_r is the vertical wind speed. For convenience, (u, v, w) are used to refer to the wind speed component (u_r, v_r, w_r) after rotation.

We analyzed the time series of meteorological elements $\overline{f}(\mathrm{t})$ such as the wind speed (u, v, w). In general, $f(\mathrm{t})$ can be divided into two parts: the low-frequency signal $\overline{f}(\mathrm{t})$ and the pulsation value superimposed on the low-frequency signal $f'(\mathrm{t})$:

$$f(\mathrm{t}) = \overline{f}(\mathrm{t}) + f'(\mathrm{t}), \tag{5}$$

where $\overline{f}(\mathrm{t})$ is the so-called "base flow" or "average flow" with a period >10 min, and $f'(\mathrm{t})$ is the turbulent fluctuation, which is turbulent fluctuation with a period <10 min.

For the turbulence kinetic energy, friction velocity and drag coefficient,

$$E' = A'^2 \equiv \frac{\overline{u'^2} + \overline{v'^2} + \overline{w'^2}}{2}, \tag{6}$$

$$u_*^2 = \left[\left(\overline{u'w'} \right)^2 + \left(\overline{v'w'} \right)^2 \right]^{1/2}, \tag{7}$$

$$u_*^2 = C_d \bar{u}^2, \tag{8}$$

where A' is the intensity of the disturbance.

4 Characteristics of the boundary layer during typhoons

Research on wind profiles over land has shown that the profile of typhoons in the surface layer can be described quantitatively by a logarithmic law. By contrast, Cheng et al. (2014) analyzed the observational data for Typhoon Hagupit and found that the near-surface typhoon wind speed was no longer a logarithmic profile over the sea. The wind speed in each layer from 10 to 100 m is roughly equal. We found that the change in the wind direction during the landfall of Typhoons Koppu, Chanthu, and Hato had an important influence on the vertical distribution of the wind speed. Unlike Typhoon Hagupit, the wind profile of Typhoon Koppu clearly shows shear before and after landfall (Figure 4b and red circle part in Figure 5b). This is because the winds were blowing from the land (Figure 6b and Figure 7) and were therefore affected by the land boundary layer and had a relatively large shear. By contrast, Typhoon Chanthu made landfall on the south side of the observational point (Figure 3) and the winds were almost always blowing from the sea (Figure 6c and Figure 7). The wind shear was the same as Typhoon Hagupit. The changes in wind speed at different heights were small and there was no obvious wind shear especially the wind speed is $< 15\text{m s}^{-1}$ (Figure 4c, Figure 5c).

Typhoon Hato was similar to Typhoon Koppu and made landfall on the north side of the observation point (Figure 3). Like Typhoon Koppu, the wind blew from the land before and after landfall (Figure 6a and Figure 7) and the wind shear was greater than that of the onshore wind over sea (Figure 4d and Figure 5a). Therefore the wind profile of a typhoon that makes landfall is divided into two types. When landfall occurs on the north side of the observation point, it is an offshore wind and the wind speed may be sheared (e.g., Typhoons Koppu and Hato). By contrast, when landfall is on the south side of the observation point, the wind blows from the sea and the wind shear is small (e.g., Typhoons Chanthu and Hagupit).

The typhoons made landfall at a certain distance from the observation position (Figure 3). Typhoons Hato and Koppu made landfall on the northeastern side of the offshore platform. After landfall, the center of the wind continued to move to the observation position, the wind speed continued to increase, and the wind direction began to rotate by 360° after landfall. During landfall, the wind speeds were the same in all layers and Typhoons Hato and Koppu had a large wind speed gradient in the eyewall area. At this time, the wind was affected by the underlying surface of the land and the wind speed shear was large (Figure 5a, b). The wind direction of Typhoons Koppu and Hato was offshore before landfall and the wind direction rotated counterclockwise after landfall and became an onshore wind after <228 °(Figure 6a, b). Typhoon Chanthu made landfall on the southwestern side of the offshore platform. The wind direction was always onshore so the wind shear was small (Figure 5c and Figure 6c).

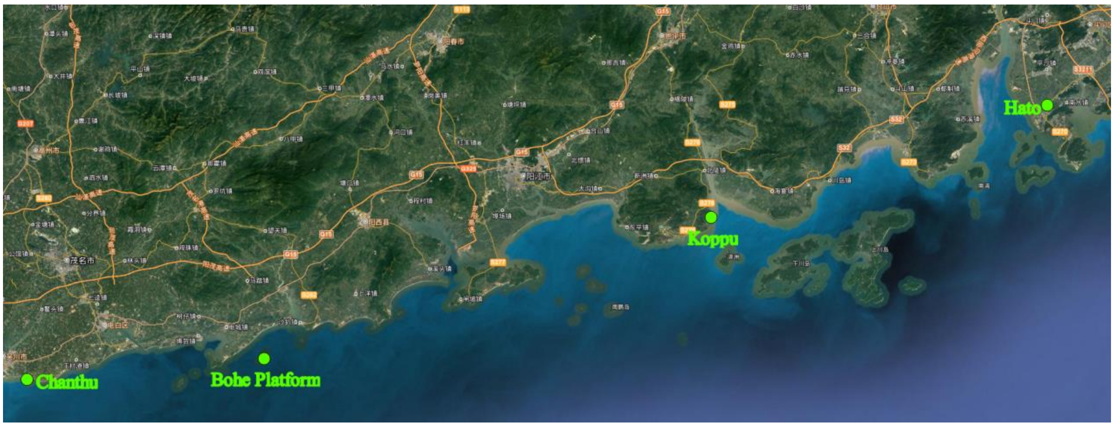

Figure 3. Location of typhoon landfall sites.

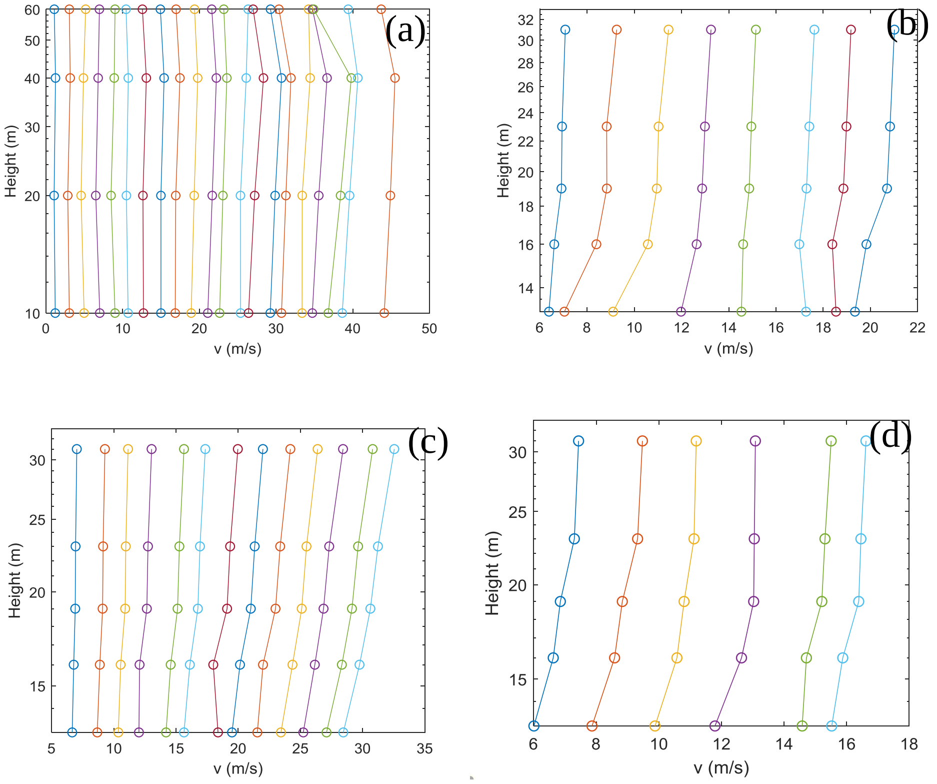

Figure 4. Typhoon 10-min mean wind profiles. **(a)** Typhoon Hagupit, 22–26 September 2008; **(b)** Typhoon Koppu, 13–17 September 2009; **(c)** Typhoon Chanthu, 20–24 July 2010; and **(d)** Typhoon Hato, 21–25 August 2017.

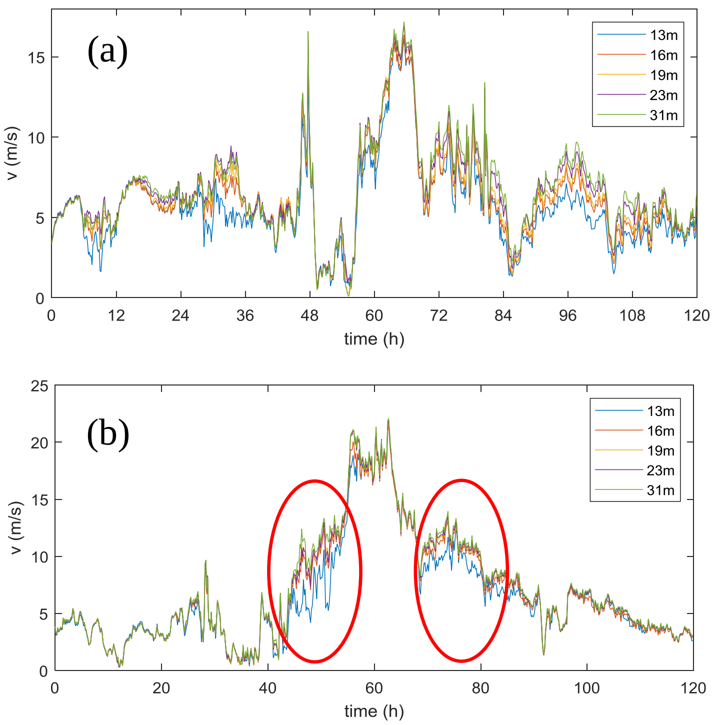

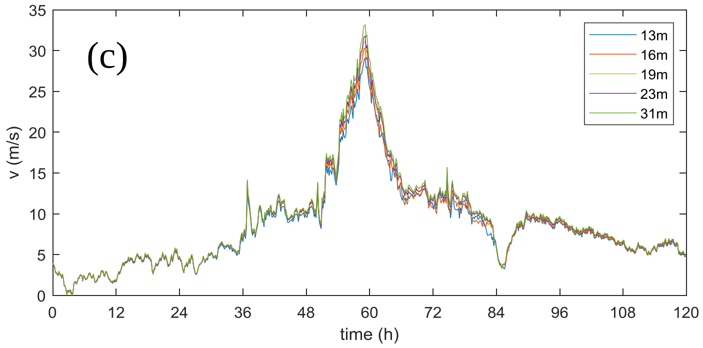

Figure 5. Time series of the 10-min averaged horizontal velocity at five levels measured by cup anemometers on the platform. **(a)** Typhoon Hato, 21–25 August 2017; **(b)** Typhoon Koppu, 13–17 September 2009; and **(c)** Typhoon Chanthu, 20–24 July 2010.

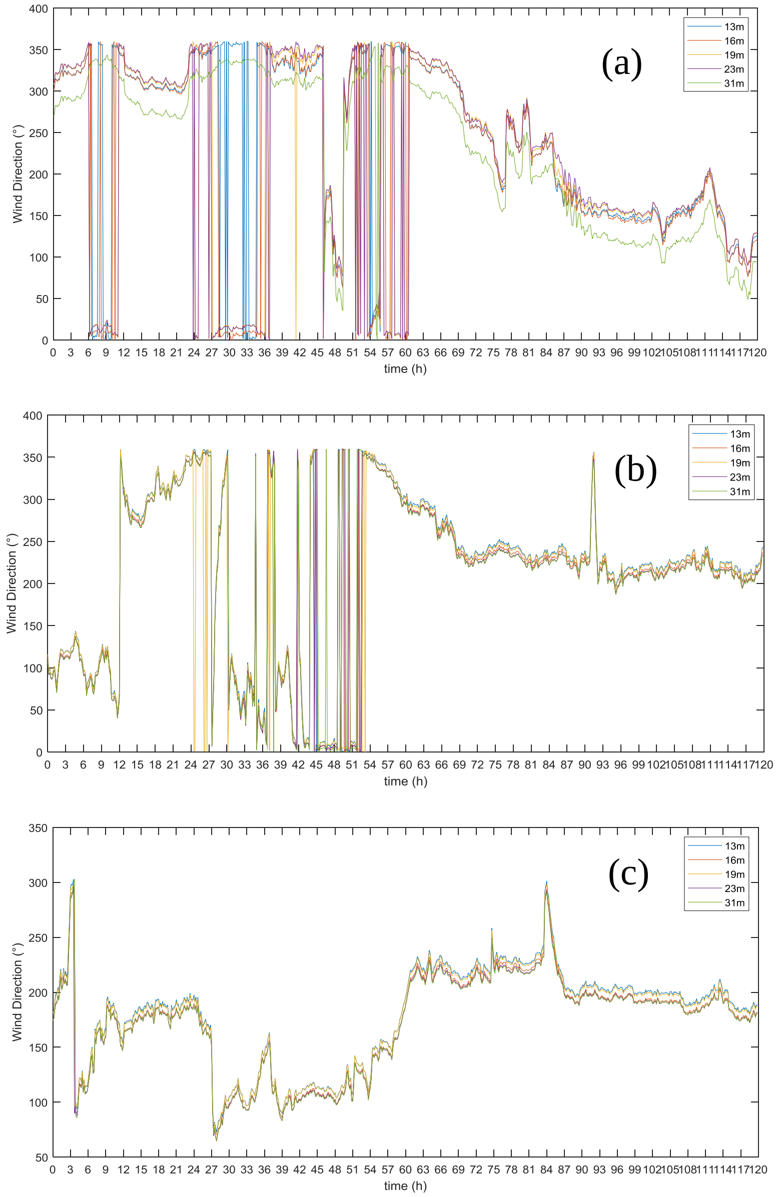

Figure 6. Time series of the wind direction of Typhoon. **(a)** Typhoon Hato, 21–25 August 2017; **(b)** Typhoon Koppu, 13–17 September 2009; and **(c)** Typhoon Chanthu, 20–24 July 2010

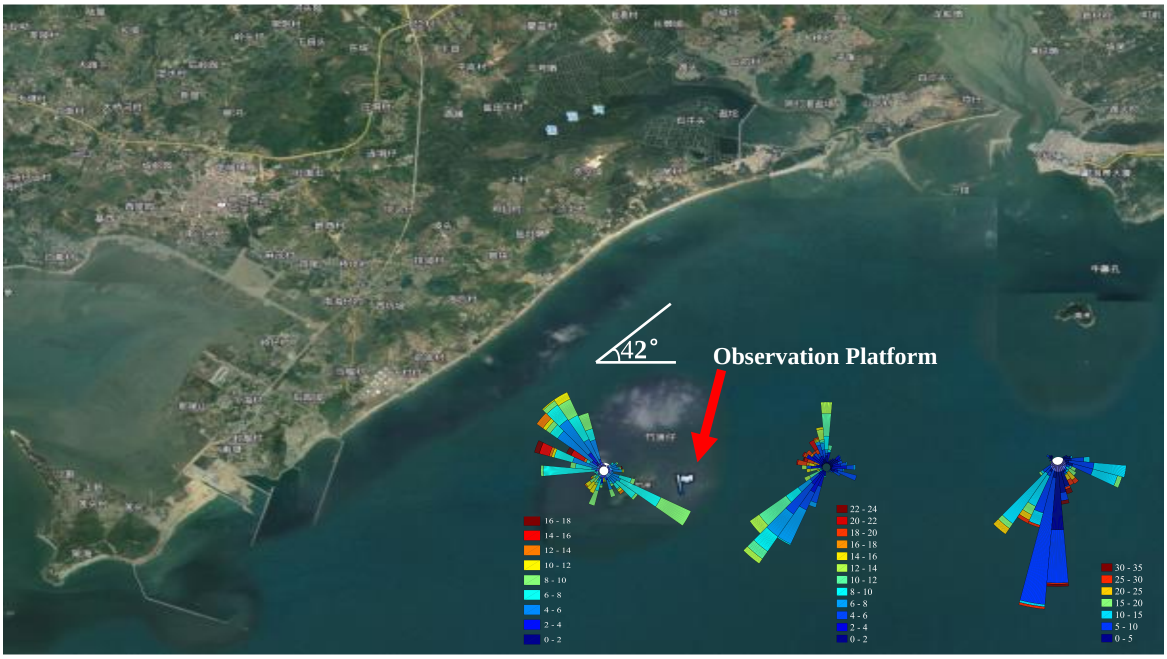

Figure 7. Wind speed roses of Typhoons Hato (left), Koppu (center), and Chanthu (right).

5 Turbulence and flux characteristics during the typhoon period

In strong winds, u_* and U_{10} are generally considered to a linear relationship. Foreman and Emeis (2010), Andreas et al. (2012), Edson et al. (2013) reported a linear coefficient form 0.051 to 0.062 in the linear regression. For offshore observation points, the properties of the underlying surface (roughness) can be considered as anisotropic under strong winds, and the variation relationship of turbulence statistics with wind speed varies with the incoming direction. Analysis shows that, in the case of sea breeze, its slope 0.052 (Figure 11c) agrees with the studies of Foreman and Emeis (2010), Andreas et al. (2012), And Edson et al. (2013). However, the change of turbulence statistics with wind speed depends not only on the direction of incoming wind but also on where the typhoon made landfall.

The relationship between the intensity of the turbulence fluctuation (standard deviation) and the wind speed of Typhoon Koppu was analyzed by the onshore and offshore winds before, during, and after landfall. We found that the intensity of the turbulence fluctuation showed a clear bifurcation with the change in wind speed. The onshore and offshore winds do not completely match the bifurcation (Figure 8a). If they are distinguished by before, during, and after landfall, with the time of landfall defined as two hours before and after landfall, then the bifurcation of the turbulence fluctuation intensity with wind speed matches well with that before and after landfall. The diagonal line connecting the two branches corresponds to the time of landfall (Figure 8b). Therefore the intensity of the turbulence fluctuation changed from A to B before Typhoon Koppu made landfall and the intensity of the turbulence fluctuation changed from B to C when it made landfall. The wind speed decreased after landfall and the intensity of the turbulence fluctuation returned from C to A.

Further more, gusts and turbulence are different in strong winds. High-frequency turbulence is nearly isotropic, whereas gust disturbance has an anisotropic coherent structure. As typhoons are strong winds, we used the method of decomposition and analyzed the wind speed for strong wind (Zeng et al., 2010). Based on this, we subdivided f' into two parts: turbulent fluctuation with a period of <1 min $f_t(\mathrm{t})$ and gust disturbances with a period >1 min and <10 min $f_g(\mathrm{t})$.We therefore divided $f(\mathrm{t})$ into three parts according to the period (frequency) by Fourier expansion:

$$f(\mathrm{t}) = \overline{f}(\mathrm{t}) + f_g(\mathrm{t}) + f_t(\mathrm{t}), \tag{9}$$

where $\overline{f}(\mathrm{t})$ is the so-called “base flow” or “average flow” with a period >10 min. The turbulence kinetic energy can be decomposed into two parts: $E' = E_g + E_t$, where E_g is the energy of the gust disturbance and E_t is the energy of the turbulent fluctuation.

For the friction velocity and drag coefficient,

$$u_{\mathrm{g}*}^2 = \left[\left(\overline{u_{\mathrm{g}} w_{\mathrm{g}}} \right)^2 + \left(\overline{v_{\mathrm{g}} w_{\mathrm{g}}} \right)^2 \right]^{1/2},$$

$$u_{\mathrm{t}*}^2 = \left[\left(\overline{u_{\mathrm{t}} w_{\mathrm{t}}} \right)^2 + \left(\overline{v_{\mathrm{t}} w_{\mathrm{t}}} \right)^2 \right]^{1/2} \tag{10}$$

where $u_g(\mathrm{t})$, $v_g(\mathrm{t})$, $u_t(\mathrm{t})$, and $v_t(\mathrm{t})$ are the gust disturbance and turbulence fluctuations along and perpendicular to the mean wind direction.

$$u_{g*}^2 = C_{dg}\bar{u}^2,$$

$$u_{t*}^2 = C_{dt}\bar{u}^2, \tag{11}$$

where g represents the gust and t is the turbulence.

The intensity of the gust disturbance was also bifurcated (Figure 8d). The scatter points at each moment in the gust disturbance graph are more scattered as a result of the influence of the underlying surface and thermal disturbance. The turbulent friction velocity is similar to the turbulence fluctuation intensity, but the turbulent friction velocity after landfall is relatively messy and then enters the lower branch of the bifurcation as the wind speed decreases (Figure 9a). If the turbulent friction velocity after landfall is distinguished by offshore and onshore winds, then the friction velocity of a typhoon is chaotic when it makes landfall during an offshore wind and appears more regular during an onshore wind (Figure 9b). Unlike the intensity of turbulent fluctuation, this law only depends on whether a typhoon makes landfall; the law for the turbulent friction velocity is more complex.

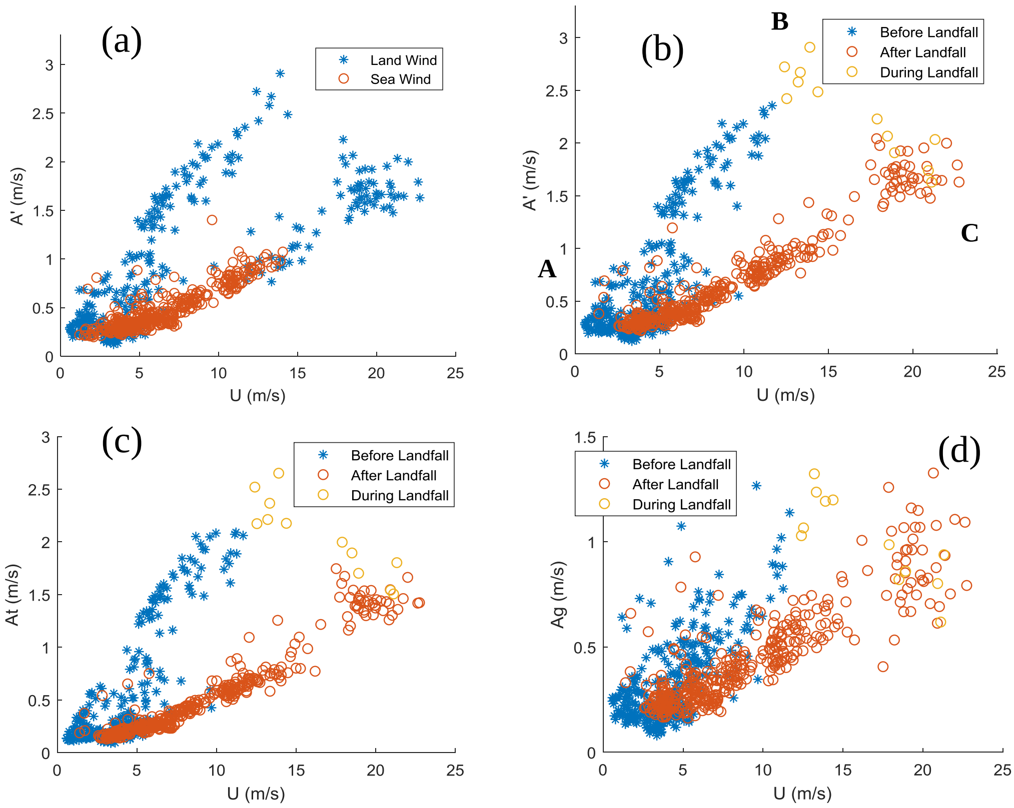

Figure 8. Fluctuation intensity and wind speed relationship of Typhoon Koppu during an offshore wind at 27 m on 13–17 September 2009: **(a)** total intensity during land wind and sea wind; **(b)** total intensity before, during and after landing; **(c)** turbulent fluctuation intensity; and **(d)** gust disturbance intensity.

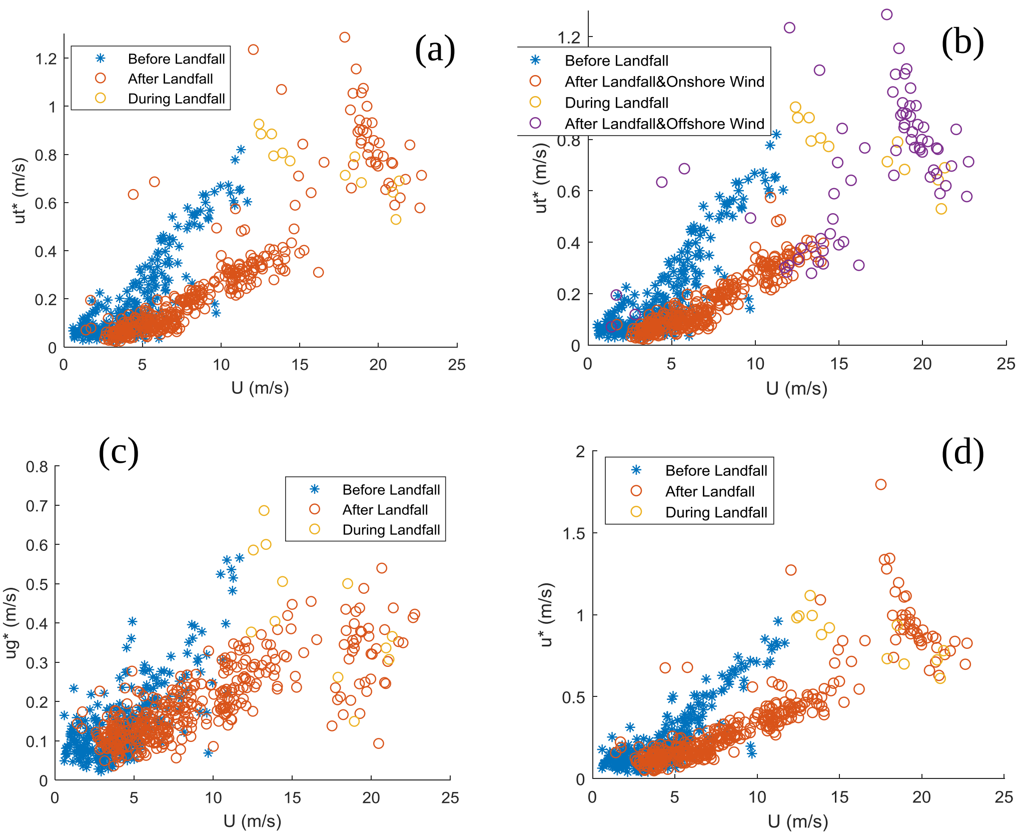

Figure 9. Friction velocity and wind speed relationship of Typhoon Koppu before and after landfall. **(a)** Turbulence friction velocity. **(b)** Turbulence friction velocity, which changes with the onshore and offshore wind speeds after landfall. **(c)** Gust friction velocity. **(d)** Total friction velocity.

Figure 10 shows the turbulent disturbance intensity-wind speed time series of Typhoon Chanthu. Unlike Typhoon Koppu, the turbulence intensity scatter points move along a curve, as do the gust disturbance intensity, turbulent friction velocity, gust friction velocity, and friction velocity. The gust disturbance scatter points are also relatively scattered (Figure 10c). These differences from Typhoon Koppu can be explained by the fact that the observation point for Typhoon Chanthu is on the north side of the landing point and the flow is almost an onshore wind both before and after landfall (Figure 6c and Figure 7).

Typhoon Hato is the same as Typhoon Koppu. The observation point is on the south side of the landfall site. The intensity of the turbulence fluctuation, gust disturbance intensity, and gust friction velocity are similar to those of Typhoon Koppu. They show bifurcations and the branches correspond to before, during, and after landfall (Figures 12). The turbulent friction velocity, gust friction velocity, and total friction velocity are similar to those of Typhoon Koppu. The turbulent friction velocity is scattered in the offshore wind after landfall and the scattering point of the onshore wind is more regular (Figure 13).

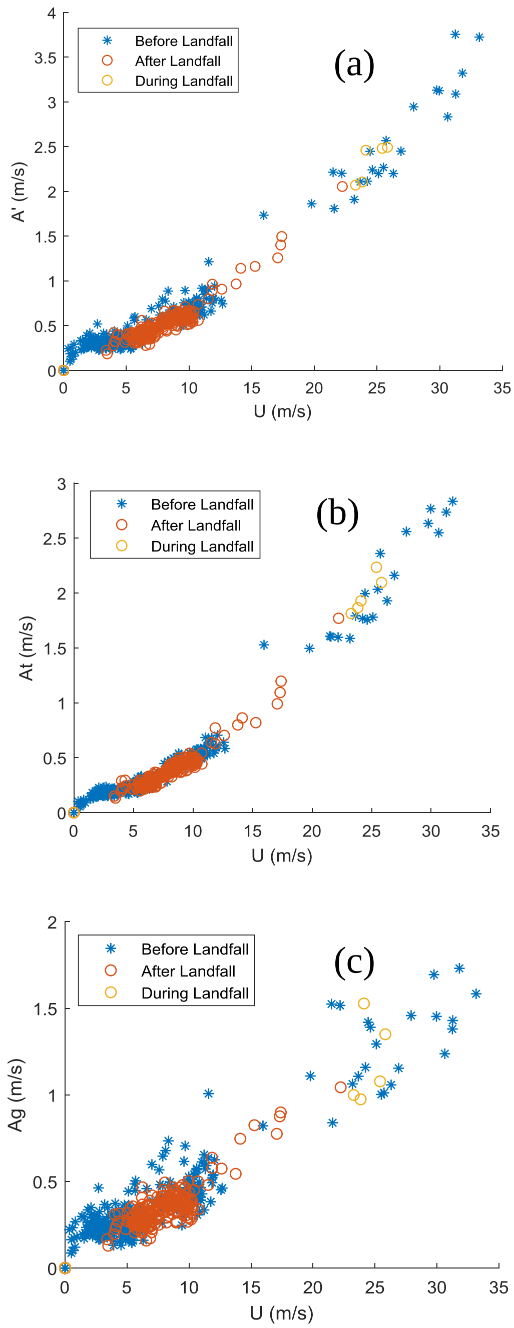

Figure 10. Fluctuation intensity and wind speed relationship at 27 m for Typhoon Chanthu before and after landfall on 20–24 July 2010: **(a)** total intensity; **(b)** turbulent fluctuation intensity; **(c)** gust disturbance intensity;

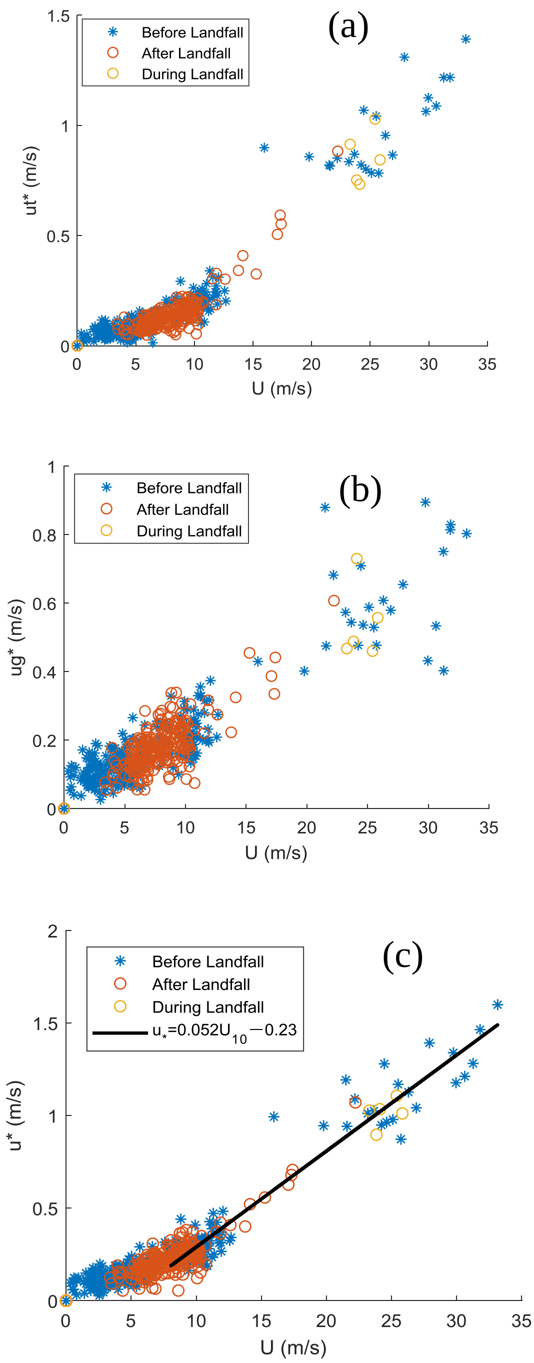

Figure 11. Friction velocity and wind speed relationship at 27 m for Typhoon Chanthu before and after landfall on 20–24 July 2010: **(a)** Turbulence friction velocity. **(b)** Gust friction velocity. **(c)** Total friction velocity.

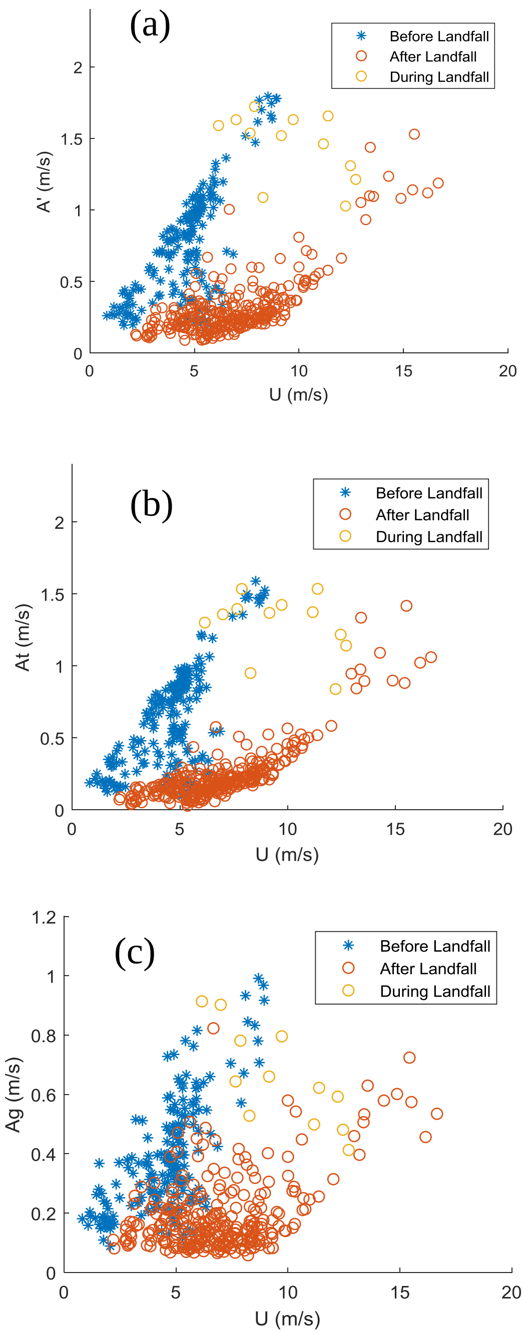

Figure 12. Fluctuation intensity and wind speed relationship at 27 m for Typhoon Hato before and after landfall on 22–25 August 2017: **(a)** total intensity; **(b)** turbulent fluctuation intensity; **(c)** gust disturbance intensity;

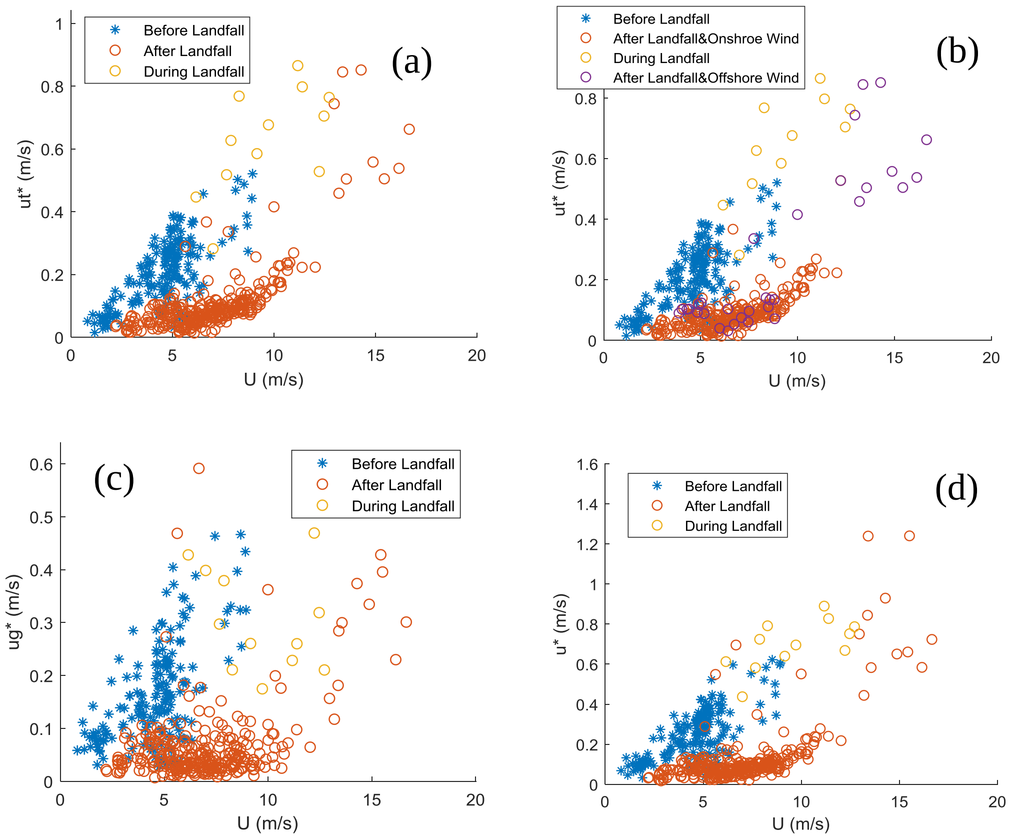

Figure 13. Friction velocity and wind speed of Typhoon Hato before and after landfall. **(a)** Turbulence friction velocity. **(b)** Turbulence friction velocity, which changes with the onshore and offshore wind speeds after landfall. **(c)** Gust friction velocity. **(d)** Total friction velocity.

The turbulence fluctuation intensity, gust disturbance intensity, and friction velocity of a typhoon making landfall are therefore divided into two categories: typhoons that make landfall on the north side of the observation point and typhoons that make landfall on the south side of the observation point. For typhoons in the first category, the disturbance intensity moves along a triangle on the disturbance intensity-wind speed graph. The three sides correspond to before, during, and after landfall. The friction velocity is more complex. Before landfall, it moves along one branch and moves from one branch to the other during landfall. After landfall it is scattered in the offshore wind and, after the wind direction changes to an onshore wind, the friction velocity enters the lower branch on the friction velocity-wind speed graph. By contrast, for typhoons that make landfall on the south side of the observation point, almost all the wind comes from the sea and the gust-turbulence disturbance intensity and friction velocity move along a curve on the corresponding wind speed graph.

6 Discussion and conclusions

The turbulence fluctuation intensity of Typhoons Koppu and Hato have different curves before and after landfall. By contrast, the turbulence fluctuation intensity of Typhoon Chanthu is the same both before and after landfall and is similar to that of Typhoons Koppu and Hato after landfall (Figure 14b). This means that, although the underlying surfaces are different, the relationship between the turbulent fluctuation intensity and the wind speed is the same. This shows that the relationship between the turbulent fluctuation and the wind speed depends not only on the nature of the underlying surface, but also on whether the typhoon has made landfall. Figure 14d shows that the turbulent friction velocities of Typhoons Koppu, Hato, and Chanthu increase with wind speed after landfall.

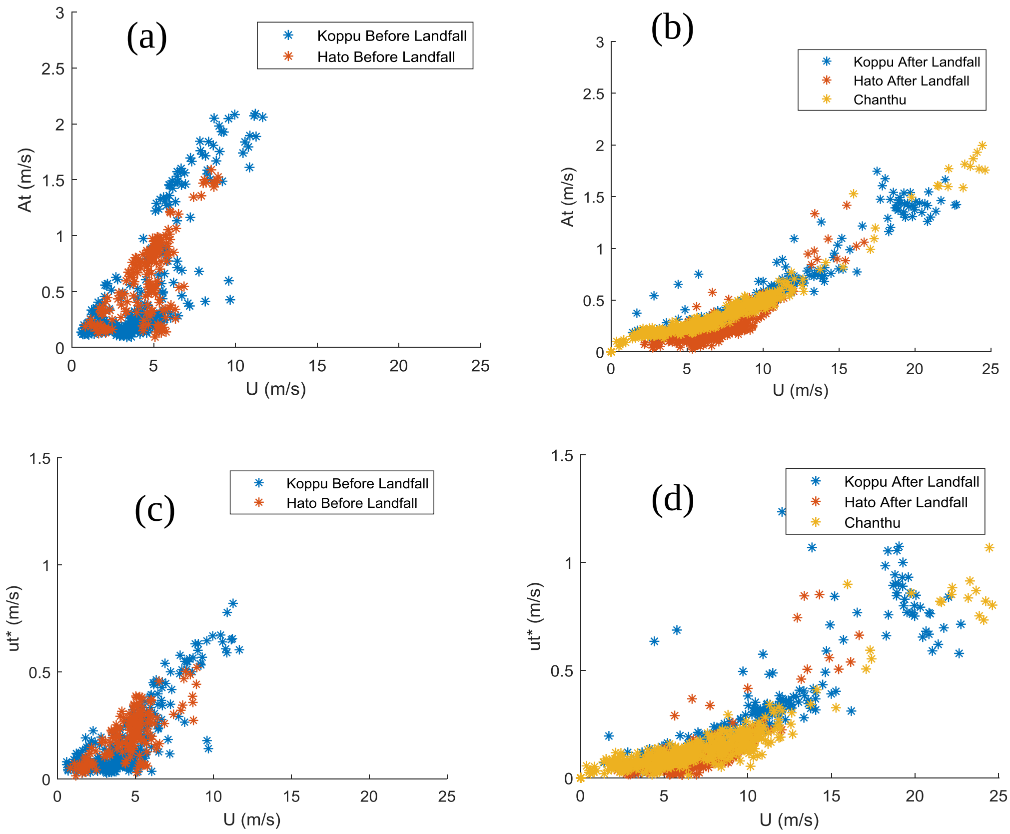

Figure 14. Turbulent fluctuation intensity–wind speed relationship **(a)** before and **(b)** after landfall and the friction velocity–wind speed relationship **(c)** before and **(d)** after landfall.

The time series of the wind speed, friction velocity, drag coefficient, and temperature difference of Typhoon Koppu (Figure 15) show that the friction velocity and drag coefficient change as the wind speed changes before and after the typhoon makes landfall. The friction velocity and drag coefficient decrease with increasing wind speed during landfall, but increase with increasing of wind speed before and after landfall. The figure also shows the temperature difference between the upper and lower layers. The temperature of the lower layer is higher than the temperature of the upper layer during the whole period of the typhoon, and the boundary layer is weakly unstable. The disturbance intensity and friction velocity vary with the wind speed. The points on the turbulence fluctuation graph are concentrated, whereas the points on the gust disturbance graph are more scattered and disordered (Figures 8–13). This may be because low-frequency gusts are easily affected by the terrain and heat. For example, the disturbance of the temperature difference in Figure 15 causes the disturbance in C_{dg}. This kind of disturbance in C_{dg} (a deviation from the average value) is shown as the point dispersion of the gust friction velocity on the friction velocity-wind speed map.

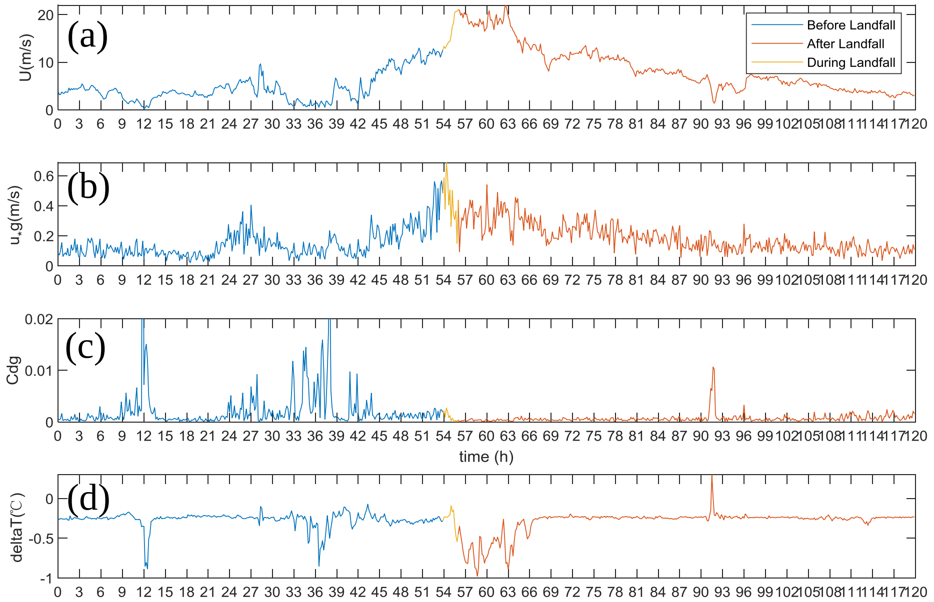

Figure 15. (a) Wind speed, **(b)** friction velocity, **(c)** drag coefficient and **(d)** temperature difference before and after landfall of Typhoon Koppu on 13–17 September 2009.

We studied the effect of the relative positions of where the typhoon made landfall and the observation point and the change in the wind direction and position on the mean wind, turbulence fluctuation intensity, and friction velocity in the typhoon boundary layer. We discuss the regularity of the spatial distribution of these variables and the evolution of their spatial distribution over time.

Before the typhoon made landfall (Figure 16a), observation point A experienced an onshore wind. The wind speeds in the surface layer were roughly equal. Point A′ over the sea was similar. The observation point B experienced an offshore wind and the wind profile changed from the logarithmic profile of the offshore wind to the inner boundary layer of the ocean, so shear sometimes occurred at point B. There was clearly shear at point B′ on land. The turbulence fluctuation intensity of points A and A′changed with the wind speed in accordance with the relationship for turbulence over the sea surface, which is the lower branch of the bifurcation. The turbulence fluctuation intensity of point B changed with the wind speed in the upper branch of the bifurcation. The frictional velocity was the same as the turbulence fluctuation intensity.

When the typhoons made landfall (Figure 16b), points A and A′ recorded onshore winds and the wind speeds in the surface layer were roughly equal. Point B was an offshore wind, affected by the land, and the near-surface wind speed at point B sometimes showed shear. The turbulent fluctuation intensity at points A and A′ continued in the lower branch, whereas the turbulent fluctuation intensity of B changed from the upper branch (before landfall) to the lower branch (after landfall). The friction velocity was similar.

After the typhoons had made landfall (Figure 16c and 16d), the observation points A and A′ recorded onshore winds and the wind speeds in the surface layer were roughly equal. The wind speed in the surface layer at point B sometimes showed shear of the offshore wind (Figure 16c) and at another times indicated an onshore wind (Figure 16d). At points A and A′, the turbulent fluctuation intensity stayed within the lower branch. The change in the turbulence fluctuation intensity at point B with wind speed was in the lower branch of the bifurcation and the variation in the turbulence fluctuation intensity with wind speed was the same whether the wind was offshore or onshore. At points A and A′, the friction velocity changed with the wind speed and stayed in the lower branch. At point B, the change in the friction velocity with wind speed was more complex. At landfall, the friction velocity changed with the wind speed from the upper to the lower branch and the change in the friction velocity with the wind speed appeared chaotic. At this time, the wind was offshore. If the typhoon center continued to penetrate the land, the offshore wind became an onshore wind at point B (Figure 16d) and the friction velocity was concentrated and entered the lower branch.

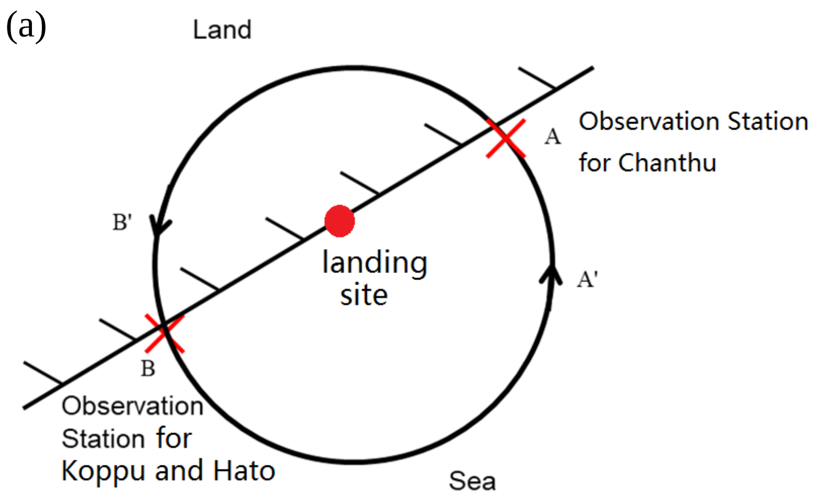

(b)

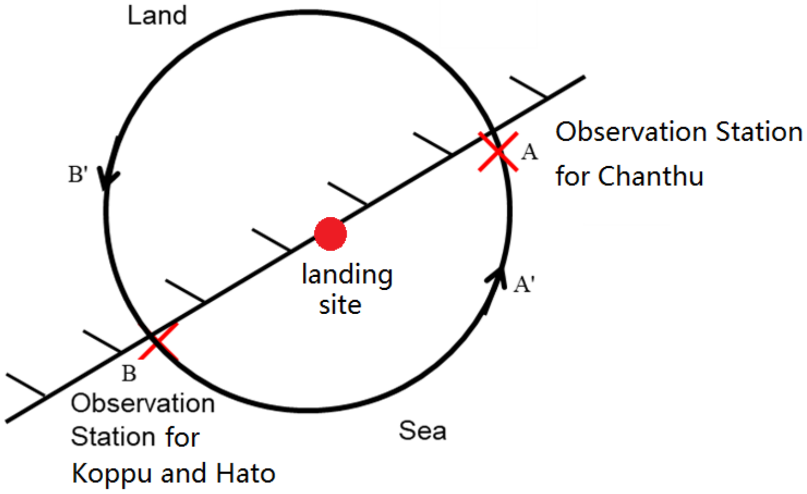
Land
B'
Observation Station
for Chanthu
A
landing
site
A'
B
Observation
Station for
Koppu and Hato
Sea

(c)

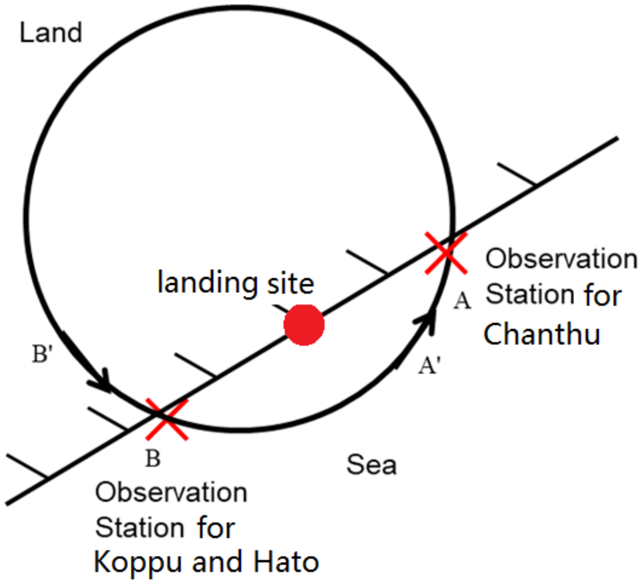
Land
landing site
Observation
Station for
Chanthu
A
B'
A'
B
Observation
Station for
Koppu and Hato
Sea

(d)

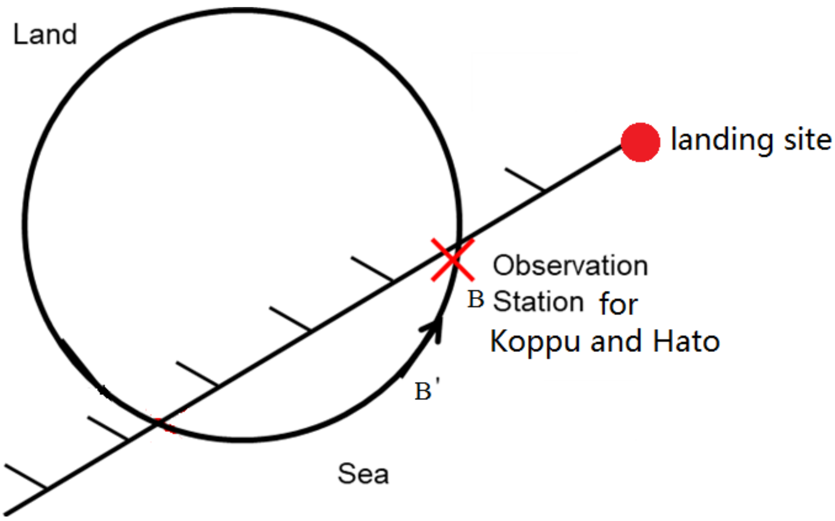
Land
landing site
Observation
B Station for
Koppu and Hato
B'
Sea

Figure 16. Schematic diagrams of the typhoons (a) before landfall, (b) at landfall, and (c) after landfall with offshore and onshore winds at the observation station and (d) after landfall with an onshore wind at the observation station.

By studying the mean field and turbulence in the boundary layer during typhoon landfall using data from a platform 6.5 km offshore, we found that:

1. The wind profile of the offshore wind is different from the wind profile of the onshore wind. Sometimes there is obvious shear in the offshore wind, whereas the onshore wind has almost no shear.

2. For typhoons making landfall on the northeast side of the observation point, the relationship between the turbulence fluctuation intensity and wind speed diverged as a result of the influence of the landfall site. The typhoons making landfall on the southwestern side of the observation point were onshore before and after landfall and moved along a curve.

3. The friction velocity and drag coefficient follow similar rules, but lack in regularity during offshore winds after landfall.

4. The turbulence intensity, friction velocity, and drag coefficient decrease during landfall with increasing wind speed.

5. After landfall, Typhoon Chanthu experienced onshore winds, whereas Typhoons Koppu and Hato sometimes experienced offshore winds and sometimes onshore winds, although the turbulence fluctuation intensity all conformed to the same curve.

Acknowledgments

This work was supported by the National Science Foundation of China under Grant 41630530 and 42175103, the National Key Research and Development Plan from the Ministry of Science and Technology of China under Grant 2018YFC0213102, the National Key Scientific and Technological Infrastructure project "Earth System Science Numerical Simulator Facility" (EarthLab). The data is available at https://pan.baidu.com/s/1MOxxX6tnxYZS4VJnsd592Q. Password:2n49.

References

Andreas, E. L., & Decosmo, J. (1999). Sea spray production and influence on air–sea heat and moisture fluxes over the open ocean. In G. Geernaert (Ed.), *Air–sea flux: momentum, heat, and mass exchange*. Dordrecht: Kluwer.

Bi, X., Gao, Z., Liu, Y., Liu, F., Song, Q., Huang, J., et al. (2015). Observed drag coefficients in high winds in the near offshore of the South China Sea. *Journal of Geophysical Research Atmospheres*, *120*, 6444–6459.

Cao, S. Y., Tamura, Y., Kikuchi, N., Saito, M., Nakayama, I., Matsuzaki, Y. (2009). Wind characteristics of a strong typhoon. *Journal of Wind Engineering and Industrial Aerodynamics*, *97*, 11–21.

Cheng, X. L., Wu, L., Song, L. L., et al. (2014). Marine–atmospheric boundary layer characteristics over the South China Sea during the passage of strong Typhoon Hagupit. *Journal of Meteorological Research*, *28*(3), 420–429.

Donelan, M. A. (1990). Air–sea interaction. In B. Le Mehaute & D. M. Hanes (Eds.), *The sea*. Ocean Engineering Science (pp. 239–292). Wiley.

Donelan, M. A., Dobson, F. W., Smith, S. D., & Anderson, R. J. (1993). On the dependence of sea surface roughness on wave development. *Journal of Physical Oceanography*, *23*, 2143–2149.

Drennan, W. M., Graber, H. C., Hauser, D., & Quentin, C. (2003). On the wave age dependence of wind stress over pure wind seas. *Journal of Geophysical Research*, *108*(C3), 8062.

Fang, P., Zhao, B., Zeng, Z., Yu, H., Lei, X., & Tan, J. (2018). Effects of wind direction on variations in friction velocity with wind speed under conditions of strong onshore wind. *Journal of Geophysical Research: Atmospheres*, *123*, 7340–7353.

Foken, T., & Wichura, B. (1996). Tools for quality assessment of surface-based flux measurements. *Agricultural and Forest Meteorology*, *78*, 83–105.

Gao, Z. Q., Ma, Y. M., Wang, J. M., & Zhang, Q. R. (2000). Studies on roughness lengths, neutral drag coefficients and bulk transfer coefficients over Nansha islands sea area [in Chinese]. *Tropical Oceanology*, *19*(1), 38–43.

Garratt, J. R. (1977). Review of drag coefficients over oceans and continents. *Monthly Weather Rev*iew, *104*, 418–442.

Geernaert, G. L. (1987). Measurements of the wind stress, heat flux, and turbulence intensity during storm conditions over the North Sea. *Journal of Geophysical Research*, *92*(C12), 13127–13139.

Harper, B., Kepert, J., & Ginger, J. (2008). *Wind speed time averaging conversions for tropical cyclone conditions*. Paper presented at the 28th Conference on Hurricanes and Tropical Meteorology, American Meteorological Society, Orlando, FL.

Hock, T. R., & Franklin, J. L. (1999). The NCAR GPS dropwind sonde. *Bulletin of the American Meteorological Society*, *80*, 407–420.

Ishizaki, H. (1983). Wind profiles, turbulent intensities and gust factors for design in typhoon-prone regions. *Journal of Wind Engineering and Industrial Aerodynamics*, *13*, 55–66.

Johnson, H. K., Hojstrup, J., Vested, H. J., & Larsen, S. E. (1998). On the dependence of sea roughness on wind waves. *Journal of Physical Oceanography*, *28*, 1702–1716.

Lange, B., Johnson, H. K., Larsen, S., Hojstrup, J., Kofoed-Hansen, H., & Yelland M. J. (2004). On detection of a wave age dependency for the sea surface roughness. *Journal of Physical Oceanography*, *34*(6), 1441–1458.

Large, W. G., & Pond, S. (1981). Open ocean momentum flux measurements in moderate to strong winds. *Journal of Physical Oceanography*, *11*, 324–336.

Ma, X. G., & Hu, F. (2004). Prediction of atmospheric pollutant concentrations using support vector machines [in Chinese]. *Progress in Natural Science*, *14*(3), 349–353.

Powell, M. D., Vickery, P. J., & Reinhold, T. A. (2003). Reduced drag coefficient for high wind speeds in tropical cyclones. *Nature*, *422*, 279–283.

Quan, L. H., Hu, F., & Cheng, X. L. (2007). Analyses of probability distribution and its statistical characters of turbulent scalars in atmospheric boundary layer [in Chinese]. *Acta Meteorological Sinica*, *65(1),* 105–112.

Smith, S. D. (1988). Coefficients for sea surface wind stress. *Journal of Geophysical Research*, 93(C12), 15467.

Smith, S. D., Anderson, R. J., Oost, W. A., Kraan, C., Maat, N., De Cosmo, J., et al. (1992). Sea surface wind stress and drag coefficients: The HEXOS results. *Boundary-Layer Meteorology*, *60*, 109–142.

Sparks, P. R. (2003). Wind speeds in tropical cyclones and associated insurance losses. *Journal of Wind Engineering and Industrial Aerodynamics*, *91*, 1731–1751.

Sparks, P. R., & Huang, Z. (2001). Gust factors and surface-to-gradient wind-speed ratios in tropical cyclones. *Journal of Wind Engineering and Industrial Aerodynamics*, *89*, 1047–1058.

Song, L. L., Chen, W. C., Wang, B. L., Zhi, S. Q., & Liu, A. J. (2016). Characteristics of wind profiles in the landfalling typhoon boundary layer. *Journal of Wind Engineering and Industrial Aerodynamics*, *149*, 77–88.

Stewart, R. W. (1974). The air–sea momentum exchange. *Boundary-Layer Meteorology*, *6*, 151–167.

Tamura, Y. , Iwatani, Y. , Hibi, K. , Suda, K. , Nakamura, O. , & Maruyama, T. , et al. (2007). Profiles of mean wind speeds and vertical turbulence intensities measured at seashore and two inland sites using doppler sodars. *Journal of Wind Engineering & Industrial Aerodynamics*, 95(6), 411-427.

Taylor, P. K., & Yelland, M. J. (2001). The dependence of sea surface roughness on the height and steepness of the waves. *Journal of Physical Oceanography*, *31*, 572–590.

Toba, Y., Iida, N., Kawamura, H., Ebuchi, N., & Jones, I. S. F. (1990). Wave dependence of sea-surface wind stress. *Journal of Physical Oceanography*, *20*, 476–492.

Vickers, D., & Mahrt, L. (1997). Quality control and flux sampling problems for tower and aircraft data. *Journal of Atmospheric and Oceanic Technology*, *14*, 512–526.

Vickery, P. J., & Skerlj, P. F. (2000). Elimination of exposure D along the hurricane coastline in ASCE 7. *Journal of Structural Engineering*, *126*, 545–549.

Wu, J. (1980). Wind-stress coefficients over sea surface near neutral conditions – A revist. *Journal of Physical Oceanography*, *1*0, 727–740.

Yelland, M., & Taylor, P. K. (1996). Wind stress measurements from the open ocean. *Journal of Physical Oceanography*, *26*, 541–558.

Zeng, Q. C., Cheng, X. L., Hu, F., & Peng, Z. (2010). Gustiness and coherent structure of strong winds and their role in dust emission and entrainment. *Advances in Atmospheric Sciences*, *27*(1), 1–13.

Zhao, Z. K., Gao, Z. Q., Dan, L., Bi, X. Y., Liu, C. X., & Liao, F. (2013). Scalar flux–gradient relationships under unstable conditions over water in coastal regions. *Boundary-Layer Meteorology*, *148*, 495–516.

Zhao, Z. K., Liu, C. X., Li, Q., Dai, G. F., Song, Q. T., & Lv, W. H. (2015). Typhoon air-sea drag coefficient in coastal regions. *Journal of Geophysics Research Oceans*, *120*(2), 716–727.